



Utilization of e-waste as a silica source for the synthesis of the catalyst support MCM-48 and highly enhanced photocatalytic activity of supported titania nanoparticles

Tzong-Horng Liou*, Bo-Chen Lai

Department of Chemical Engineering, Ming Chi University of Technology, 84 Gungjuan Rd., Taishan, New Taipei 24301, Taiwan

ARTICLE INFO

Article history:

Received 3 August 2011

Received in revised form

12 December 2011

Accepted 15 December 2011

Available online 23 December 2011

Keywords:

E-waste

Titania

MCM-48

Photocatalyst

Mesoporous structure

ABSTRACT

An extensive range of studies has investigated the silica-supported TiO₂ catalyst. However, research on cubic-type MCM-48 photocatalyst materials is limited. E-waste represents one of the fastest-growing sources of industrial waste worldwide. The present study reports, for the first time, direct synthesis of TiO₂ nanoparticles loaded on MCM-48 deriving from e-waste. Alkali-extracted electronic packaging resin ash provided a source of sodium silicate precursors. Titanium salts were introduced into the pores of MCM-48 and subsequently decomposed to TiO₂ nanoparticles. Methylene blue was used to evaluate the photoactivity of the hybrid catalyst at varying amounts of TiO₂ loading, catalyst masses, and heat-treatment temperatures. Results indicated that TiO₂/MCM-48 demonstrates a combined effect, including the photocatalytic activity of TiO₂ along with the high adsorptive efficiency of MCM-48. Different ratios of titanium metal deposited on silica surfaces had significant influences on the porosity and adsorption properties of the MCM-48 support, as well as the dispersion, particle size, and catalytic activity of the TiO₂ catalyst. Good dispersion of TiO₂ on the MCM-48 support played a significant role in obtaining high photocatalytic activity. Synthesis of mesoporous photocatalysts from e-waste using a green approach can reduce the disposal problem and produce viable materials for a wide range of applications.

© 2011 Elsevier B.V. All rights reserved.

1. Introduction

Nanosized TiO₂ particles are highly efficient catalytic agents for decomposition of organic pollutants commonly found in industrial wastewater [1] and hazardous gases [2]. The high photocatalytic activity of TiO₂ nanoparticles makes these materials good candidates for the synthesis of novel materials for applications such as hydrogen storage materials [3], dye-sensitized solar cells [4], and biomaterials [5]. However, the small size of bare TiO₂ (approximately 30 nm) limits its photocatalytic efficiency because aggregation of the TiO₂ particles has the effect of decreasing surface area [6]. Removing such a small sized catalyst incurs high filtration costs post-reaction [7]. Therefore, achieving good dispersion of TiO₂ immobilized on support materials with high surface area is critical for obtaining high photocatalytic efficiency. The high-ordered M41s represent excellent catalyst supports because these materials contain high internal surface areas, large pore volumes, and large nanoscale pores [8,9]. MCM-41, MCM-48, and MCM-50 are the main members in the M41s family, having hexagonal, cubic, and unstable lamellar structures, respectively. Owing to its

three-dimensional pore channels, which can provide more favorable mass transfer kinetics than MCM-41, MCM-48 is an attractive candidate for application as a catalyst support [10]. However, few investigations have evaluated MCM-48 due to highly sensitive synthetic conditions [11].

The electronics industry is one of the world's fastest-growing manufacturing industries. The worldwide revenue for the semiconductor industry exceeded US \$226 billion in 2009, and is expected to increase by a further 13% per year in the future [12]. However, this industry generates an estimated 20–50 million tons of electronic and electrical waste (e-waste), such as old computers, mobile phones, television sets, stereos, and radios, on an annual basis [13]. These electronic products use large amounts of epoxy molding compounds (EMCs) as protective packaging materials, for example integrated circuits (IC) packaging [14]. Typically, the main constituents of packaging resin material are epoxy resin, phenol resin, and silica [15]. The residual resins generated during the electronic packaging process constitute more than 30–50 wt% of the total resin compound. Consumers rapidly replace electronic goods with newer models, generating increasing amounts of resin waste. Currently, the main methods for treatment of e-waste are reuse, remanufacturing, recycling, incineration, and landfilling [16]. However, plastic materials are essentially non-biodegradable therefore disposal in landfills is not a practical solution, further adding to

* Corresponding author. Tel.: +886 2 29089899x4617; fax: +886 2 29083072.

E-mail address: thliou@mail.mcut.edu.tw (T.-H. Liou).

the waste problem. Packaging resin waste is rich in silica (approximately 80 wt%) [17]. Recycling of silica from e-waste is, therefore, important in terms of waste treatment and also the recovery of economically viable raw materials for MCM-48 mesoporous molecular sieve and photocatalyst composite production.

To prevent the TiO_2 nanoparticles from aggregating previous studies used zeolites [18], mesoporous silica (MCM-41, SBA-15, and MCF) [19–23], and activated carbons [24] to increase the photocatalytic efficiency of TiO_2 . Some studies used solid wastes, such as coal fly ash and rice husk, as silica sources for MCM-41 type photocatalyst production [25,26]. However, limited studies have investigated the cubic-type MCM-48 photocatalyst materials. The phase characteristics of MCM-48 are strongly influenced by reaction conditions [27,28]. Bandyopadhyay et al. [29] synthesized MCM-48 containing TiO_2 nanoparticles using a wet impregnation method. Results showed the successful deposition of nanosized TiO_2 particles inside the pores of the MCM-48 matrix without destroying their integrity. Zhao et al. [30] evaluated the photocatalytic activities of titanium-containing MCM-48. Synthesis of the photocatalyst included the addition of a titanium precursor before or after the addition of tetraethylorthosilicate (TEOS). Adding the titanium precursor after the TEOS produced highest hydrogen evolution by photocatalytic activity under UV irradiation. Zanjanchi et al. [7] incorporated tungstophosphoric acid- TiO_2 into MCM-41 and observed that the strong adsorptive capacity of the hybrid catalyst combined with its photocatalytic activity to rapidly remove methylene blue.

The present study investigated a mesoporous photocatalyst consisting of TiO_2 nanoparticles dispersed on MCM-48 materials. The MCM-48 was prepared using sodium silicate precursors, obtained from recycled products of electronic packaging resin wastes. Commercial fabrication of sodium silicate from quartz sand and sodium carbonate at 1300 °C requires a large amount of energy [31]. In contrast, sodium silicate extracted from electronic packaging resin wastes is inexpensive, providing an economical silicon source for large-scale production of MCM-48. In previous studies, the MCM-41 silica synthesized from recycling of electronic packaging resin wastes used a cationic surfactant as template [32]. The present study's procedures included the deposition of TiO_2 within the pores of MCM-48 in two major steps. First, the analysis of the optimal conditions for obtaining catalyst support MCM-48 from packaging resin waste using neutral and cationic surfactant mixtures. Second, the impregnation of TiO_2 nanoparticles on MCM-48 supports using a sol-gel method. The photocatalytic activity of the hybrid photocatalyst for methylene blue degradation was investigated in detail. Various analytical methods, such as field-emission scanning electron microscope, X-ray diffractometer, Fourier infrared spectrometer, surface area analyzer, inductively coupled plasma-mass spectrometer, element analyzer, and thermogravimetric analyzer characterized the MCM-48 support and TiO_2 /MCM-48 composite. The MCM-48 support, with high surface area, provided an environment for TiO_2 dispersion which is highly favorable for the degradation of organic wastes. The synthesis of photocatalyst composites via a green approach can potentially provide a means of recycling and limit further increases in e-waste.

2. Experimental

2.1. Chemicals

2.1.1. Reagents for mesoporous silica molecular sieve synthesis

Electronic packaging resin wastes used in this study were provided by an electronic packaging mill (Siliconwave Precision Co., Taiwan). The basic constituents and properties of the resin material were as previously described by Liou [15]. The following reagent-grade chemicals were used as received: cetyltrimethylammonium

bromide (CTAB, $\text{C}_{16}\text{H}_{33}(\text{CH}_3)_3\text{NBr}$, Acros Organics), polyethylene glycol dodecyl ether ($\text{C}_{12}(\text{EO})_4$, Sigma-Aldrich), sodium hydroxide (NaOH, Merck), hydrochloric acid (HCl, Merck), sulfuric acid (H_2SO_4 , Merck), and air (Sun Fu Co., 99.995%).

2.1.2. Reagents for TiO_2 /PRA-MCM-48 photocatalyst synthesis

The following reagent-grade chemicals were used as received: titanium butoxide ($\text{Ti}(\text{OBu})_4$, Acros Organics), isopropanol (Sigma-Aldrich), acetylacetone (TCI Co., Tokyo), nitric acid (HNO_3 , Merck), methylene blue (MB, Acros Organics), and silica gel (surface area 400 m^2/g , Acros Organics).

2.2. Preparation of mesoporous silica molecular sieve

Packaging resin ash (PRA) was prepared using a thermal decomposition technique according to Liou's methods [17]. The resin wastes were ground, burned in air, and then leached using HCl solution to remove metallic impurities. The solid was filtered and washed with distilled water to obtain PRA raw material for mesoporous silica fabrication. Sodium silicate was prepared from PRA using the alkali-extracting method. The PRA was mixed with 4.0 M NaOH solution and boiled at 100 °C for 6 h. The solution was centrifuged and filtered several times using a glass filter (Whatman plc, England) to remove small quantities of residues. The solution was then diluted to 2.0 M using deionized water.

For typical silica molecular sieve synthesis, 1.82 g of CTAB and 0.27 g of $\text{C}_{12}(\text{EO})_4$ were dissolved in 32 ml of deionized water. Sodium silicate solution was mixed with the CTAB/ $\text{C}_{12}(\text{EO})_4$ solution with stirring. The 1.0 M H_2SO_4 solution was added dropwise to the silicate solution with constant stirring. A S20-k pH meter (Mettler Toledo) was employed to monitor the pH of the solution. The pH was adjusted with H_2SO_4 or NaOH, and the gel was loaded in a PTFE-lined stainless steel autoclave and heated for 48 h. The precipitated products were filtered, dried, calcined in air at 1 °C/min heating rate and then maintained at 550 °C for 6 h. The MCM-48 obtained from PRA by adopting optimum synthesis conditions is denoted as PRA-MCM-48.

2.3. Preparation of TiO_2 /PRA-MCM-48 photocatalyst

Samples of TiO_2 nanoparticles impregnated on PRA-MCM-48 supports were prepared using a sol-gel technique [33]. Fig. 1 presents a flow chart of the steps of the main reaction of TiO_2 -modified mesoporous silica. In a typical experiment, 10 g of $\text{Ti}(\text{OBu})_4$ was mixed with 3.532 g isopropanol and 0.029 g acetylacetone in a breaker with continuous stirring. An aqueous solution of isopropanol was added dropwise into the $\text{Ti}(\text{OBu})_4$ solution. The hydrolysis and condensation of titanium precursors were observed in the reaction system. The presence of a white precipitate indicated the formation of $\text{Ti}(\text{OH})_4$. The samples were washed with deionized water. A desired amount of PRA-MCM-48 was transferred into a breaker containing 56 g water and titanium precipitates. The slurry was stirred with known amounts of 0.5 M HNO_3 added dropwise. Then, the slurry was loaded into a glass round-bottomed flask and heated to reflux at 85 °C for 12 h. Finally, the suspension was washed with deionized water followed by filtration and centrifugation, then dried in an oven to obtain the as-synthesized photocatalyst. The photocatalyst composites were obtained by heat-treating the as-synthesized solids in air at 300–700 °C for 2 h. This sample is denoted as TiO_2 /PRA-MCM-48.

Pure TiO_2 and TiO_2 /silica-gel were synthesized the same photocatalyst preparation processes described previously except PRA-MCM-48 was not added during TiO_2 synthesis or it was replaced by commercial silica gel, respectively.

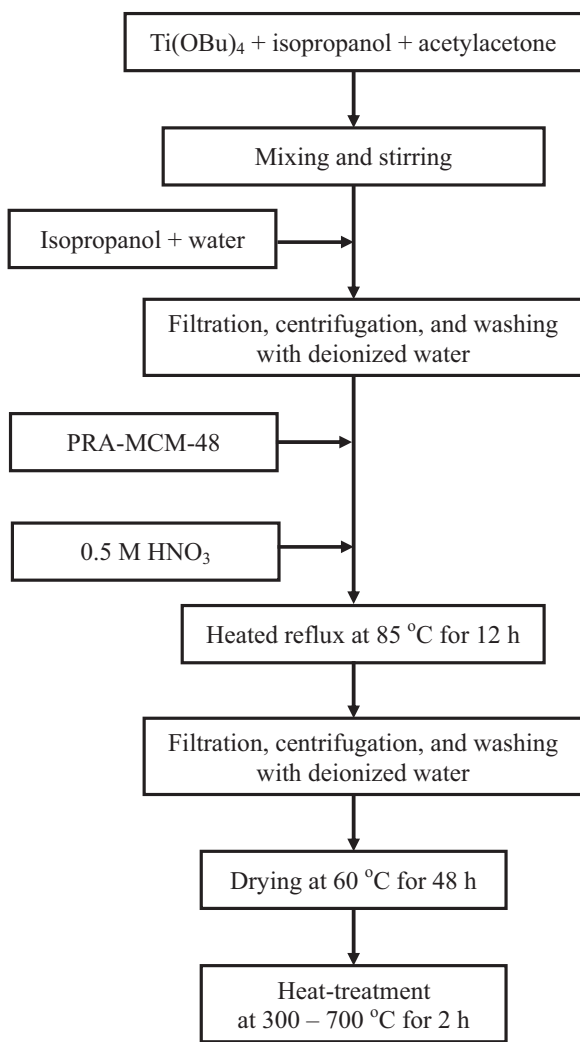


Fig. 1. Scheme of preparation of $\text{TiO}_2/\text{PRA-MCM-48}$ photocatalyst.

2.4. Photocatalytic activity measurement of catalyst material

A desired amount of PRA-MCM-48, pure TiO_2 , $\text{TiO}_2/\text{silica-gel}$, or $\text{TiO}_2/\text{PRA-MCM-48}$ was added to 200 ml of 50 μM methylene blue (MB) solution. The initial pH of the suspension was adjusted to 3.85 by diluted H_2SO_4 standard solution. Prior to irradiation, the suspensions were stirred in the dark for 15 min. A 6 W UV lamp (UVP UVG-54, working at 254 nm) was used as the light source and the suspension was constantly stirred during illumination. A specimen of the suspension was collected at given time intervals using a syringe and filtered through 0.45 μm cellulose acetate filter (Advantec, Dismic-13cp) to remove catalyst particles. All the filtrates were analyzed using a Genesys spectrophotometer (Thermo Electron Corporation). The concentration of MB was determined by measuring the absorbance at the maximum absorption peak of 666 nm. The fraction for adsorption and photodegradation of MB on the catalyst materials was calculated using: $X_{\text{MB}} = (C_0 - C)/C_0$, where C_0 and C represent the initial and instantaneous concentrations of MB, respectively.

2.5. Characterization of the silica molecular sieve and photocatalyst materials

The metallic impurities of photocatalyst samples were analyzed using an inductively coupled plasma-mass spectrometer (Kontron Plasmakon, model S-35). BET surface area and pore volume of

the silica and photocatalyst samples were measured using a N_2 adsorption-desorption analyzer (Micrometric, ASAP 2010) at liquid nitrogen temperature. The BET surface area was obtained from N_2 adsorption data, which assumes that the cross-sectional area of a nitrogen molecule is 0.162 nm^2 . Single point total pore volume was calculated at a relative pressure (P/P_0) of approximately 0.95. Pore size distribution was obtained from the desorption branch according to the Barrett-Joyner-Halenda (BJH) method. This study assumed that micropores are less than 2 nm wide, mesopores are 2–50 nm wide, and macropores are greater than 50 nm wide. The hydrophilic behavior of the samples was evaluated by measuring the water contact angle (Sindatek Instruments Co., model MagicDroplet). Five μL of water was dropped on the surface of pelletized samples, then the contact angle was observed by optical microscopy [34].

The mesophase of samples was analyzed using a small angle X-ray scattering (SAXS) system (Osmic, model PSAXS-USW-WAXS-002) and scanning angle (2θ) ranging from 0.5° to 10°. The crystalline structure of samples was determined using a powder X-ray diffractometer (PANalytical, model X'pert pro system) with $\text{Cu-K}\alpha$ radiation and scanning angle (2θ) ranging from 10° to 80°. The constitution of catalyst samples was recorded using a Fourier infrared spectrometer (Shimadzu, model FTIR-8300). The field-emission scanning-electron microscopy (FE-SEM) with energy-dispersive X-ray spectroscopy (EDS) analysis of silica molecular sieve and photocatalyst powders was obtained using a JSM-6700F (JEOL) microscope. A Mettler thermogravimetric analyzer (model TGA/SDTA851e) analyzed the probable decomposition paths of as-synthesized silica samples. Each sample was heated at 10 °C/min heating rate in air. W/W_0 represents the weight loss of the sample.

3. Results and discussion

3.1. Analysis of metallic impurities of photocatalyst samples

Table 1 displays the amounts of metallic ingredients occurring in raw resin, PRA-MCM-48, pure TiO_2 , and $\text{TiO}_2/\text{PRA-MCM-48}$ materials. The main impurities in raw resin were antimony, iron, aluminum, and chromium; of which the antimony concentration was highest. The concentrations of metals markedly reduced in the PRA-MCM-48 sample following removal of metal salts by acid-leaching, filtration, and calcination procedures during PRA-MCM-48 synthesis [32]. In various kinds of photocatalyst, the total residual amounts of metallic ingredients from pure TiO_2 were smaller than those of $\text{TiO}_2/\text{PRA-MCM-48}$. The increased amounts of impurities in the $\text{TiO}_2/\text{PRA-MCM-48}$ sample resulted from metals occurring in the PRA raw materials. Despite applying careful purification methods, these trace metals failed to be removed. The purities of pure TiO_2 and $\text{TiO}_2/\text{PRA-MCM-48}$ catalysts were 99.96 and 99.90 wt%, respectively.

3.2. Synthesis of mesoporous catalyst support

Fig. 2(a) and (b) shows the BET surface area of silica samples synthesized at pH values between 1 and 11. The surface areas decreased with increasing pH value in acidic media. In contrast, the surface areas increased with increasing pH value in alkaline media. A pH of 11 provided a maximum surface area value of 1153 m^2/g . **Fig. 2(c)** and (d) displays the mesophase characteristics of silica synthesized at various pH values. After adjustment of the solution pH to pH 1 or pH 11, the patterns exhibited three well resolved diffraction peaks at (2 1 1), (2 2 0), and (3 3 2) planes, indicating cubic MCM-48 structure [35]. Electrostatic interaction between the organic surfactant and the inorganic silica matrix in the reaction system

Table 1

Metallic ingredients analysis of raw resin, catalyst support, and photocatalyst samples.

	Metallic ingredients as oxides (ppm)										
	Na	Sb	K	P	Au	Fe	Mg	Al	Cr	Ag	Total
Raw resin ^a	240	11,800	8	96	8	5780	53	3140	1580	8	22,713
PRA-MCM-48 ^b	ND	759	ND	2	ND	124	ND	430	3	ND	1318
Pure TiO ₂	175	4	ND	53	ND	41	9	102	30	ND	414
TiO ₂ /PRA-MCM-48 ^c	69	685	ND	25	ND	91	17	87	39	ND	1013

ND means not detected.

^a Raw resin was not burnt in air.^b Silica sample was prepared from alkali-extracted PRA and gel was formed at pH 11.^c Photocatalysts were synthesized at TiO₂/PRA-MCM-48 molar ratio of 50%.

explains this finding [9]. At pH 11, the negatively charged silica species interacted with positively charged CTA⁺ micelles, leading to the formation of a cubic framework. Silica has a high-ordered mesoporous structure, and therefore high surface area. At a pH of 1, the positively charged silica species interacted with neutral micelles to reconstruct an ordered mesophase structure [36]. This also increased the surface area of the silica sample. Synthesis of silicas at pH 3–7 provided SAXS patterns showing one main diffraction peak at 1.26°. This indicated possible destruction of the surfactant micelles, a less ordered silica pore structure, and thus, markedly

decreased surface area. The pH 9 sample demonstrated SAXS patterns corresponding to (1 0 0), (1 1 0), (2 0 0), and (2 1 0) reflections, characteristic of the MCM-41 structure [32]. The material was highly ordered with hexagonal mesostructure, comprising approximately cylindrical one-dimensional pores. Experimental results indicated that MCM-48 silica is highly sensitive to gelation pH values, revealing a more stable cubic mesophase after synthesis of silica in strongly basic media. Therefore, this study conducted the remaining experiments for the preparation of PRA-MCM-48 catalyst supports at a pH of 11.

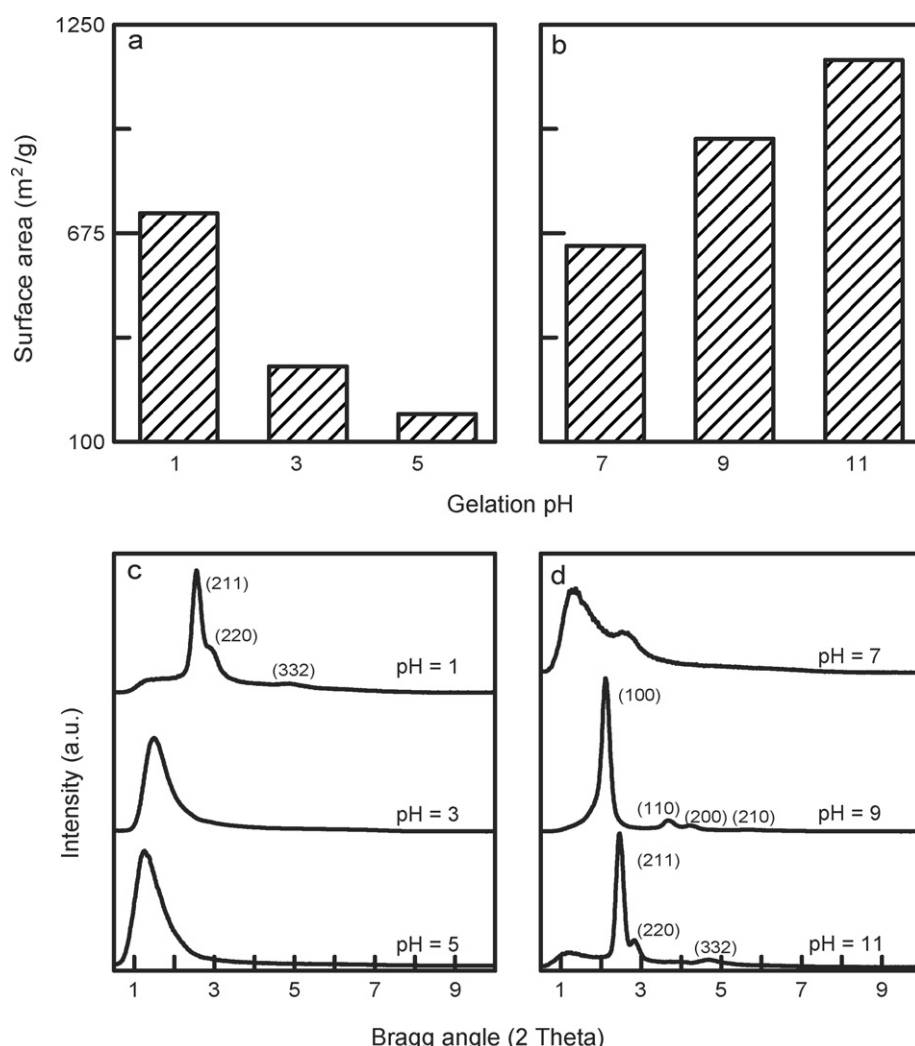


Fig. 2. Silica samples synthesized at various gelation pH values: (a) and (b) surface areas, and (c) and (d) SAXS patterns. Initial conditions: hydrothermal time, 48 h; hydrothermal temperature, 100 °C; neutral/cationic surfactant ratio, 0.13; calcination temperature, 550 °C.

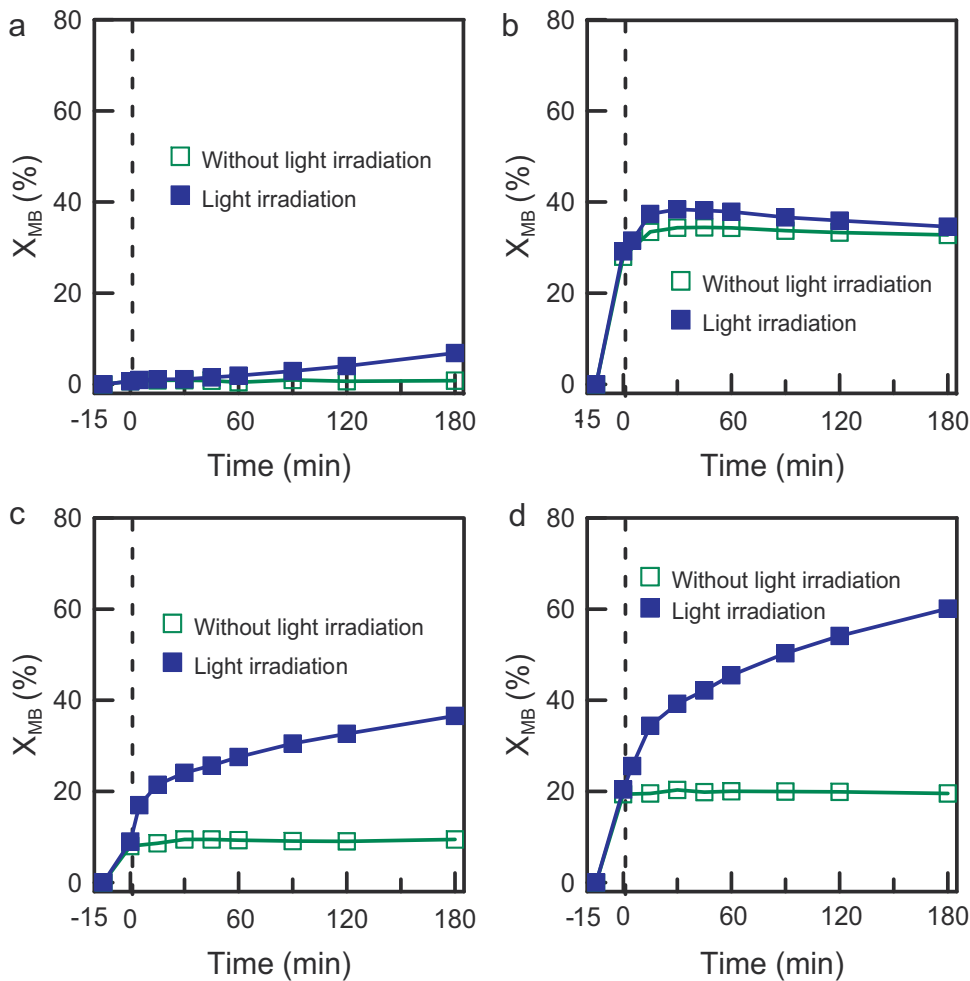


Fig. 3. Adsorption and photodegradation of methylene blue on various catalyst types: (a) pure TiO₂, (b) PRA-MCM-48, (c) 50% TiO₂/silica-gel, and (d) 50% TiO₂/PRA-MCM-48. On the left of dotted line for each figure, the removal of MB is due to adsorption at the first 15 min stirring in the dark.

3.3. Photocatalytic activity of hybrid catalyst material

3.3.1. Evaluation of catalytic performance of various types of photocatalyst

The individual and combined effects of TiO₂ and PRA-MCM-48 on photocatalytic activity are shown in Fig. 3. Two step experiments obtained the following data after mixing the catalyst with dye solution for 15 min in the dark, then exposing to UV light and irradiating for 180 min. All experiments conducted without exposure to light established the equilibrium adsorption of MB within 15 min. Following equilibrium, the concentration of MB showed no change due to the absence of photocatalytic reaction [7]. As shown in Fig. 3(a), a slight decrease in MB, caused by photodegradation, occurred after exposing pure TiO₂ to UV light for 180 min. The adsorption of MB on pure TiO₂ was insignificant indicating a low surface area and adsorption capacity, and therefore very weak photocatalytic activity. As shown in Fig. 3(b), MB sharply decreased in the initial 15 min by adding a PRA-MCM-48 in the dye solution. The MB concentration did not change after the adsorption equilibrium despite a prolonged UV exposure time of 180 min. This observation indicated that PRA-MCM-48 plays a major role in adsorption of MB. As shown in Fig. 3(c) and (d), sharp decreases in MB occurred in the initial 15 min by adding the TiO₂/silica-gel and TiO₂/PRA-MCM-48 in the dye solution, respectively. Adsorption caused these effects. Photodegradation caused successive decomposition of MB with increased UV exposure time. These observations indicated that

the hybrid catalysts' higher surface areas and adsorption capacities, compared to those of pure TiO₂, were significant factors in increased elimination of MB. Experimental results also indicated that TiO₂/PRA-MCM-48 has a higher photoefficiency than that of TiO₂/silica-gel. This will be explained in detail later in the manuscript.

3.3.2. Photodegradation of MB on TiO₂/PRA-MCM-48 catalyst

Fig. 4 shows the effects of amounts of TiO₂ loading on the photodegradation of MB at a calcination temperature of 500 °C. Increasing the TiO₂ loading markedly decreased the adsorption and photodegradation efficiencies. Aggregation of TiO₂ caused the decreases in photodegradation activity, and blocking of the outer pores of the MCM-48 catalyst support by the TiO₂ particles may have caused the decreased adsorption capacity. In contrast, low TiO₂ loading was favorable for the MCM-48, providing strong adsorbent activity sites for the adsorption of MB. This increased the MB concentration around the TiO₂ particles and enhanced the photocatalytic activity of the TiO₂ catalyst [37]. The TiO₂ particles were well dispersed in the MCM-48 matrix, preventing the TiO₂ particles from aggregating. The 30 wt% loading of TiO₂ was optimal in the TiO₂/PRA-MCM-48 catalysts. The EDS analysis of various amounts of TiO₂ loaded on the PRA-MCM48 support is shown in supplementary data (Fig. S1). The spectra confirm the presence of SiO₂ and TiO₂ as the major constituent. The spectra also reveal that decreasing SiO₂ peak intensity accompanied increased TiO₂ loading.

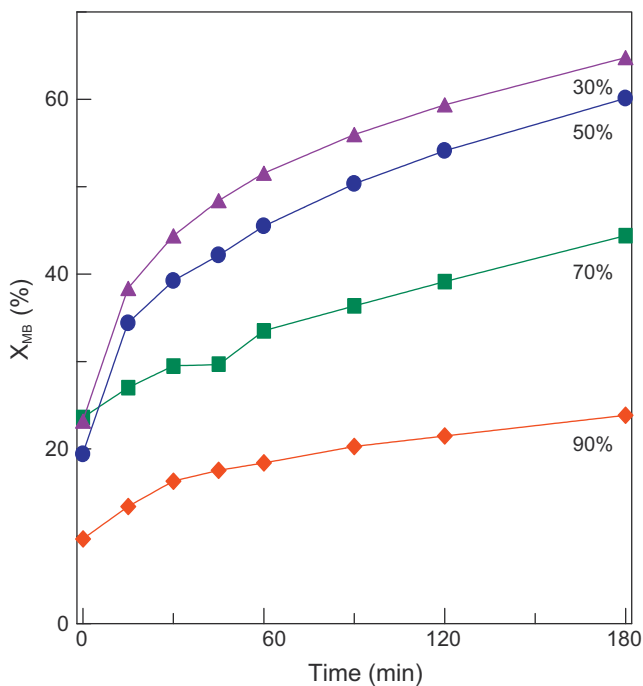


Fig. 4. Photocatalytic degradation of methylene blue for various ratios of TiO₂/PRA-MCM-48 catalyst. Initial conditions: heat-treatment temperature of catalyst, 500 °C; catalyst mass, 80 mg.

Fig. 5 shows the photocatalytic activity of MB for TiO₂/PRA-MCM-48 obtained at different heat-treatment temperatures. The adsorption efficiency and photocatalytic activity increased with increasing heat-treatment temperatures from 300 to 700 °C. This suggested that both TiO₂ catalyst crystal structure and particle size can influence the photocatalytic reaction. Wang et al. [38] investigated the composite photocatalyst of TiO₂ deposited on activated carbon at various heat-treatment temperatures. They observed that

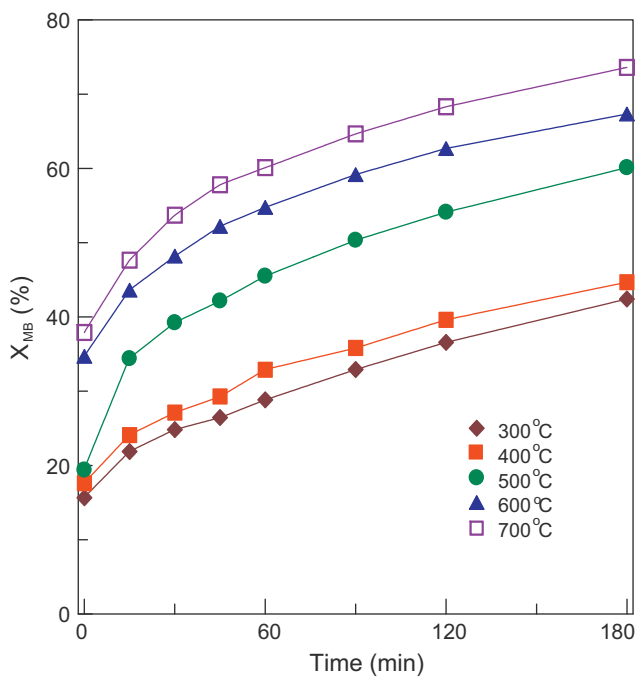


Fig. 5. Photocatalytic degradation of methylene blue on TiO₂/PRA-MCM-48 catalyst for various heat-treatment temperatures as a function of irradiation time. Initial conditions: TiO₂/PRA-MCM-48 molar ratio, 50%; catalyst mass, 80 mg.

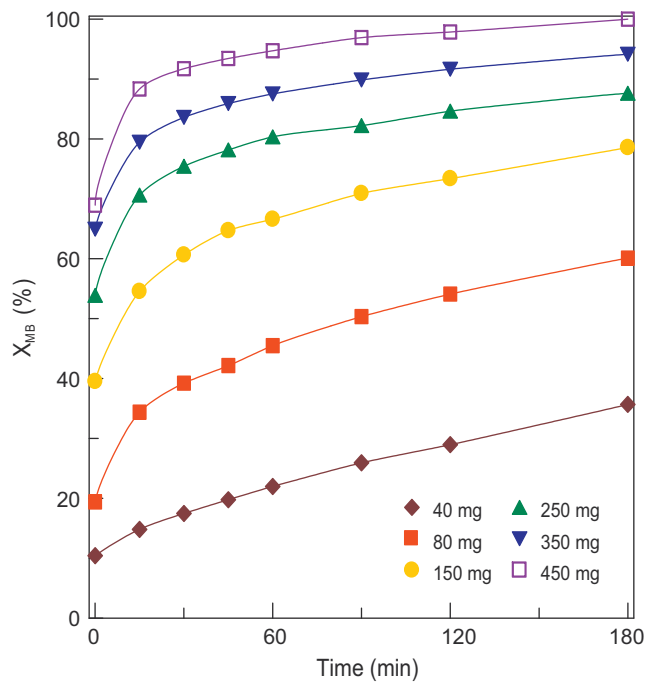


Fig. 6. Photocatalytic degradation of methylene blue on TiO₂/PRA-MCM-48 catalyst for various catalyst masses as a function of irradiation time. Initial conditions: TiO₂/PRA-MCM-48 molar ratio, 50%; heat-treatment temperature of catalyst, 500 °C.

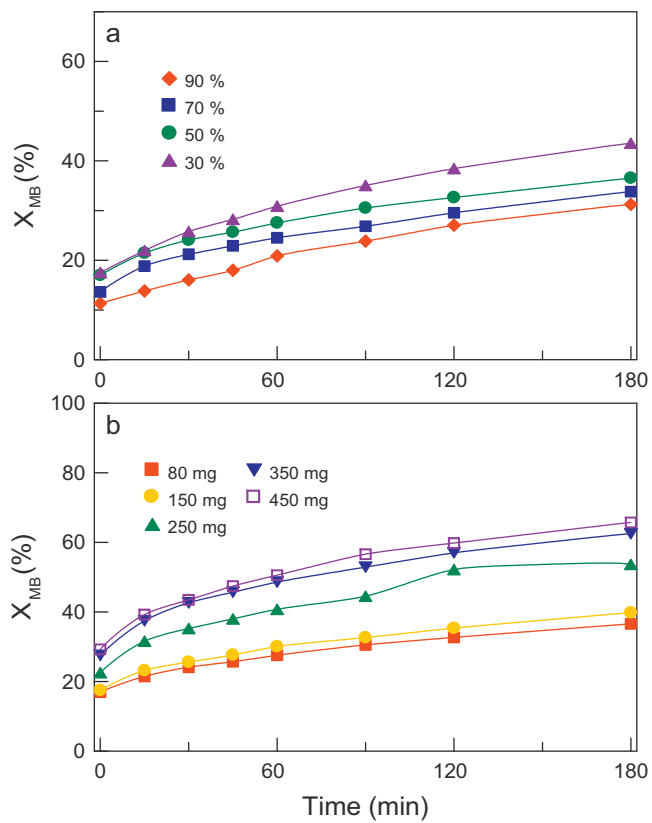


Fig. 7. Photocatalytic degradation of methylene blue on TiO₂/silica-gel catalyst: (a) TiO₂/silica-gel ratios and (b) catalyst masses.

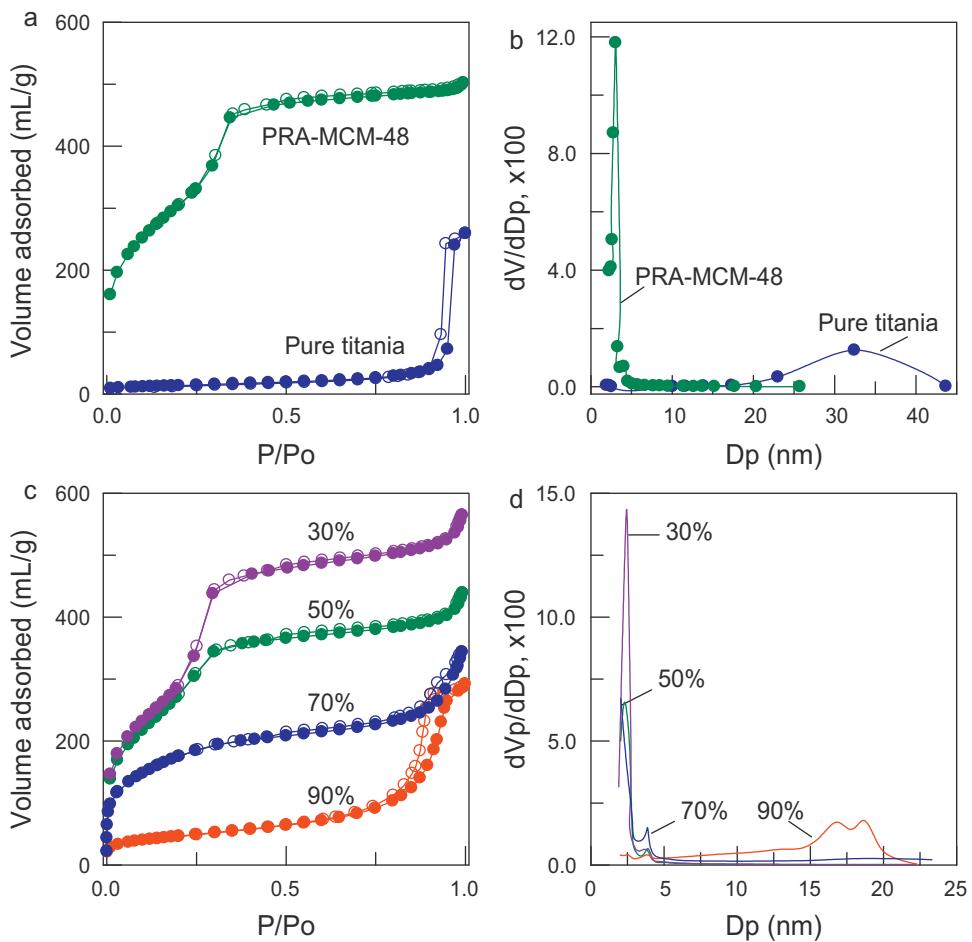


Fig. 8. Nitrogen adsorption–desorption isotherm and differential pore size distribution of photocatalyst materials: (a) and (b) pure TiO₂ and PRA-MCM-48, and (c) and (d) TiO₂/PRA-MCM-48 for various molar ratios.

higher heat-treatment temperatures favored the formation of more stable TiO₂ crystals in anatase phase. In normal circumstances, the higher the heat-treatment temperature the larger the TiO₂ particle size, and thus, the lower catalytic activity observed. Although, at 700 °C, the TiO₂ has larger particle size, the crystal structure has a greater influence on catalytic activity than catalyst particle size.

Fig. 6 shows that increasing the catalyst mass markedly increased the photodegradation of MB. Increasing the catalyst mass to 450 mg achieved a complete photocatalytic conversion of MB. The higher the catalyst mass, the higher its adsorption capacity. When catalyst mass increased to 450 mg, a sharp lowering of the MB concentration to 30% of its initial value occurred following the first 15 min stirring in the dark. At this stage, adsorption caused the elimination of the dye molecules. Experimental results revealed that the total TiO₂ content increased with increased TiO₂ loading (Fig. 4) and catalyst mass (Fig. 6). However, the photocatalytic activity decreased when TiO₂ loading increased with a fixed catalyst mass. This indicated that good dispersion of TiO₂ on the silica support is a significant factor in obtaining higher photocatalytic activity. Loading TiO₂ particles on the MCM-41 support provided similar findings [39].

To further investigate the effects of types of catalyst support on the photoefficiency of the TiO₂ catalyst, the present study prepared hybrid photocatalysts using commercial silica gel as support material. Fig. 7 presents the results of the procedures. As shown in Figs. 4, 6, and 7, the TiO₂/PRA-MCM-48 demonstrated a much higher affinity for MB adsorption and photodegradation compared with TiO₂/silica-gel. A possible explanation for TiO₂/PRA-MCM-48's

higher photocatalytic activity is the higher surface area of PRA-MCM-48, than that of silica gel, for the efficient separation of TiO₂ on the MCM-48 support. MB is a medium-sized molecule therefore relatively large MCM-48 pore sizes allow more rapid mass transfer for MB adsorption and desorption and reaction with the TiO₂ particles. This, thus, increases the rate of photocatalytic degradation.

3.4. Analysis of hybrid photocatalyst pore structure

Fig. 8 displays the N₂ adsorption–desorption isotherms of PRA-MCM-48, pure TiO₂, and TiO₂/PRA-MCM-48. Fig. 8(a) presents the isotherms of the PRA-MCM-48 and pure TiO₂ samples. At pH 11, PRA-MCM-48 is type IV. The sample showed a sharp increase in adsorbed volume at $P/P_0 = 0.2\text{--}0.4$ due to capillary condensation of nitrogen. This suggested that the pore channel size is uniform [40]. One H₂ hysteresis loop occurred at $0.4 < P/P_0 < 1.0$, indicating the formation of a mesoporous structure. The adsorption–desorption curve of pure TiO₂ contained a H₁ hysteresis loop at high relative pressure. This isotherm corresponded to type IV and the pore structure may comprise aggregates of TiO₂ particles moderately uniform in size [41]. Fig. 8(b) illustrates the pore size distribution of PRA-MCM-48 and pure TiO₂ samples. PRA-MCM-48 demonstrated a narrow peak at a pore diameter of 3.1 nm, while pure TiO₂ showed a broad pore size distribution with a peak at approximately 32.4 nm. The pore structure of pure TiO₂ mainly comprises coarse mesopores. Fig. 8(c) shows the adsorption–desorption curves of TiO₂/PRA-MCM-48 at various TiO₂ loadings. These isotherms correspond to type IV, a typical isotherm of mesoporous materials.

Table 2

Specific surface area, pore volume, and average pore diameter of PRA, catalyst support, and photocatalyst samples.

	S_{BET} (m^2/g)	V_t (cm^3/g)	V_{mic} (cm^3/g)	V_{meso} (cm^3/g)	V_{meso}/V_t (%)	D_p (nm)	Θ^d (°)
PRA ^a	2.72	0.006	0.000	0.001	16.67	51.10	–
PRA-MCM-48 ^b	1153	0.851	0.000	0.851	100.00	3.05	–
Pure TiO ₂	49	0.372	0.001	0.371	99.73	32.42	13.2
90% ^c	167	0.452	0.004	0.448	99.12	18.57	14.7
70% ^c	638	0.532	0.058	0.474	89.10	3.86	16.5
50% ^c	1016	0.638	0.079	0.559	87.62	2.32	23.4
30% ^c	1046	0.828	0.088	0.740	89.37	2.44	25.5

S_{BET} = BET surface area, V_t = total pore volume, V_{mic} = micropore volume, V_{meso} = mesopore volume. D_p = average pore diameter.

^a Raw resin was burnt in air at 5 °C/min heating rate.

^b Silica sample was prepared from alkali-extracted PRA and gel was formed at pH 11.

^c Photocatalysts were synthesized at various TiO₂/PRA-MCM-48 molar ratios.

^d Water contact angle of the catalyst samples.

The adsorbed volume increased with decreased TiO₂ loading, indicating increasing in pore volume. A well-defined step occurred in 30% and 50% TiO₂-loaded samples between $P/P_0 = 0.2$ and 0.3, indicating uniform pore size and structure. However, the isotherms of 70% and 90% TiO₂-loaded samples were not typical of MCM-48 isotherm characteristics. The 90% TiO₂/PRA-MCM-48 sample showed a hysteresis loop similar to that of pure TiO₂. Table 2 lists the surface areas, pore volumes, and average pore diameters of PRA, PRA-MCM-48, pure TiO₂, and TiO₂/PRA-MCM-48 samples. The surface area of the PRA sample was only 2.72 m^2/g and the total pore volume was 0.006 cm^3/g . The PRA sample was predominantly macroporous. The surface area of the PRA-MCM-48 was 1153 m^2/g and total pore volume was 0.851 cm^3/g . The surface area value of 49 m^2/g of pure TiO₂ approached that of commercial TiO₂ (P25) – 53 m^2/g [42]. The ratio of TiO₂ to PRA-MCM-48 significantly affected the particle size of TiO₂, as confirmed by the FE-SEM measurements. The lower the TiO₂ loading the smaller the size of the TiO₂ nanoparticles. At 30% and 50% TiO₂ loading on PRA-MCM-48, TiO₂ particles were much smaller than the pore size of PRA-MCM-48, and the total surface area of TiO₂/PRA-MCM-48 reduced by approximately 9–12%. These observations suggested that the introduction of TiO₂ into PRA-MCM-48 did not disrupt the silica pore framework. At a TiO₂ loading of higher than 50%, the TiO₂ particles were considerably larger than the pore size of PRA-MCM-48 and the dilution of TiO₂ loaded on the support had the effect of reducing the catalyst surface area. The loaded TiO₂ may, however, have blocked a proportion of the MCM-48 pore openings. This reduced the available inner catalyst surface area. Table 2 also shows that the pore structure of pure TiO₂ is predominantly mesoporous. The hybrid catalysts demonstrated increasing mesopore fractions with increased TiO₂ loading. In Fig. 8(d), the pore size distributions of TiO₂/PRA-MCM-48 catalysts reveal a narrow peak at a pore diameter of 2.4–18.6 nm, increasing with increasing TiO₂ loading. 30% and 50% TiO₂/PRA-MCM-48 had pore sizes similar to those of the PRA-MCM-48 support, indicating that TiO₂ loading did not largely affect pore structure. However, the pore size of 90% TiO₂/PRA-MCM-48 was similar to that of pure TiO₂. This suggested that the aggregation of a high proportion of TiO₂ particles on the outer pores of PRA-MCM-48 represents the main contributive factor in sample pore distribution.

Table 2 also shows the water contact angles of the pelletized samples to evaluate the hydrophilic behavior. The initial water contact angle of catalyst samples was around 13–26°, indicating a highly hydrophilic surface. A similar property is also observed by other study [34]. The high hydrophilicity of the catalysts is favorable to the increase of photocatalytic efficiency. The contact angle of the catalyst samples decreased with increasing TiO₂ loading. Though the 30% TiO₂/PRA-MCM-48 has the lowest surface hydrophilicity, its TiO₂ dispersion is the best than those high TiO₂ loading samples (as FE-SEM images indicate), leading to high photoactivity.

3.5. Characteristic analysis of silica support and hybrid photocatalyst materials

3.5.1. Analysis of crystalline structure and sample's composition

Fig. 9(a) displays the SAXS patterns of PRA-MCM-48 and TiO₂/PRA-MCM-48 catalysts at low angles. The heat-treatment temperature of the catalyst samples is 500 °C. The PRA-MCM-48 sample showed three characteristic peaks at 2.46°, 2.84°, and 4.69°, representative of the cubic phase MCM-48 structure. However,

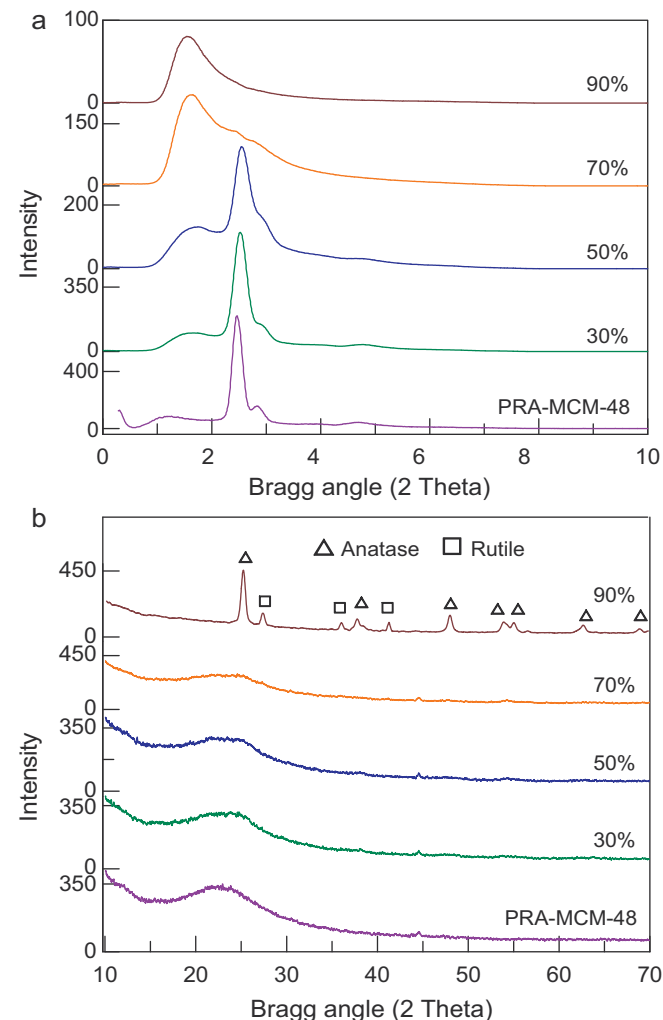


Fig. 9. X-ray diffraction patterns of PRA-MCM-48 and TiO₂/PRA-MCM-48 for various molar ratios: (a) low-angle SAXS spectra and (b) characteristics of crystalline structure.

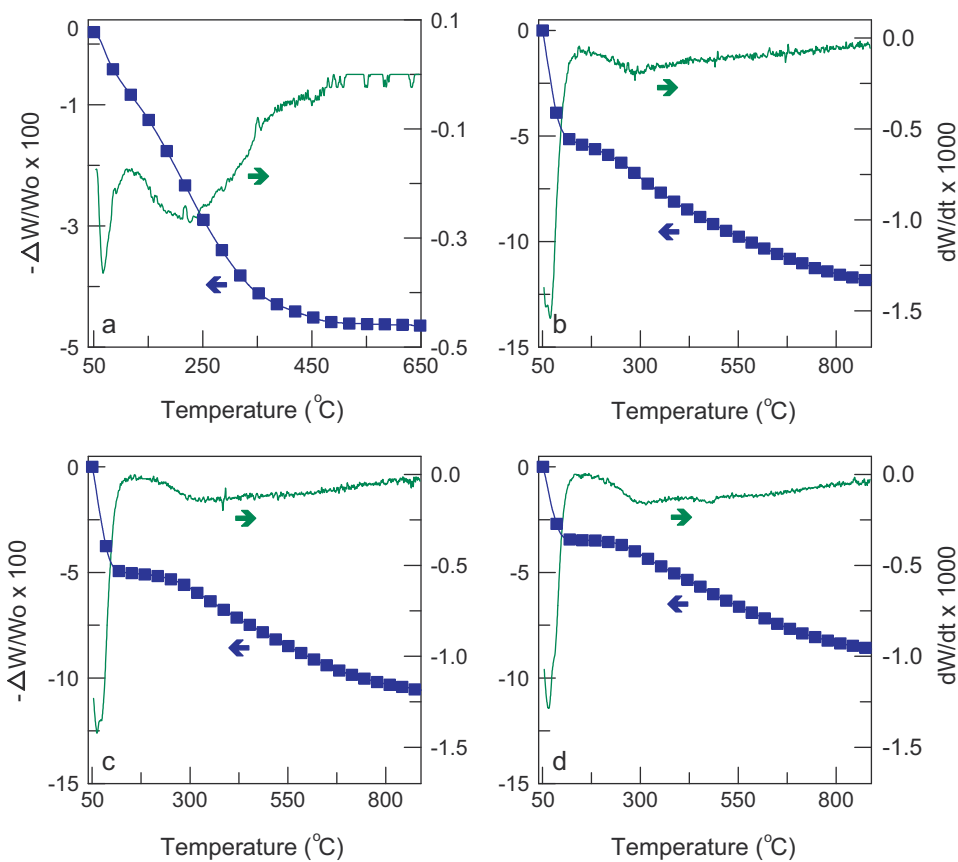


Fig. 10. TG and DTG thermograms of as-synthesized catalyst samples: (a) pure TiO_2 ; $\text{TiO}_2/\text{PRA-MCM-48}$ for various molar ratios of (b) 70%, (c) 50%, and (d) 30%, respectively.

the peak intensities of the TiO_2 -loaded samples decreased with increased TiO_2 loading. When the TiO_2 -loading increased to 70% and 90%, SAXS was unable to detect the cubic phase because the mass fraction of the MCM-48 support reduced with increasing TiO_2 . The characteristic mesophase peak at 1.54° markedly increased with increasing TiO_2 loading, due to the presence of the TiO_2 mesoporous structure. This suggested that the TiO_2 predominantly loaded on the external surface of the 70% and 90% PRA-MCM-48 samples. Fig. 9(b) displays the XRD patterns of PRA-MCM-48 and $\text{TiO}_2/\text{PRA-MCM-48}$ at higher angles. The 90% TiO_2 -loaded sample demonstrated XRD patterns mainly corresponding to anatase phase [33]. Yang et al. [43] studied the crystalline structure of TiO_2 loaded on SBA-15 and observed that the silica matrix could obstruct the anatase to rutile phase transition. When TiO_2 loading decreased to below 70%, the anatase phase could not be detected by XRD due to the small size of the TiO_2 clusters (less than $\sim 5\text{ nm}$). TiO_2 particles loaded on SBA-15 provided similar results [44]. These samples show a broad peak at $2\Theta = 25.5^\circ$ where the most intense line of the anatase pattern lines [45,46]. The PRA-MCM-48 sample demonstrated a single broad band centered at 2Θ angle of 22.5° , typically characteristic of silica, due to the presence of disordered cristobalite [47]. The FTIR spectra of PRA-MCM-48, pure TiO_2 , and $\text{TiO}_2/\text{PRA-MCM-48}$ samples are shown in supplementary data (Fig. S2). In all spectra, the peaks appeared at 1115 , 970 , 805 , and 475 cm^{-1} due to the presence of silica [32]. Wang et al. [48] observed that the presence of a $\text{Ti}-\text{O}-\text{Si}$ band led to a peak at 960 cm^{-1} in the Ti-MCM-41 sample. However, this peak is not easily observed in the IR spectrum because the $\text{Ti}-\text{O}-\text{Si}$ peak is a weak absorption band to be covered by the 970 cm^{-1} for silica solid.

Fig. 10 presents the results of thermogravimetric analyses of the as-synthesized TiO_2 and $\text{TiO}_2/\text{PRA-MCM-48}$ samples. Fig. 10(a) shows the TG and DTG curves of the as-synthesized TiO_2 sample.

The DTG curve demonstrated a peak at below 100°C , due to desorption of water molecules, a second peak at 227°C and a third peak at 356°C , both attributed to thermal decomposition of the organic substance [49]. The TG curve revealed that weight loss ceased at 470°C and, up until this temperature, total weight loss was 4.8 wt%. This indicated that a calcination temperature of 500°C was sufficient for complete removal of the organic substance. Fig. 10(b)–(d) displays the TG and DTG curves of as-synthesized $\text{TiO}_2/\text{PRA-MCM-48}$ samples obtained at various molar ratios. The reduction in mass of as-synthesized photocatalyst composites slowly decreased with increasing thermal decomposition temperature. Release of water and organic substances within PRA-MCM-48 silica may have caused the observed reductions in mass. The TG curves showing small reductions in mass at high temperature were caused by the high porosity of the silica framework. Releasing volatile matter from the silica matrix required a longer heating duration. Reductions in sample masses increased as the molar ratio of $\text{TiO}_2/\text{PRA-MCM-48}$ increased because only small amounts of volatile matter remained inside the silica matrix when loading of the titanium precursor on the PRA-MCM-48 support decreased.

3.5.2. Analysis of sample surface morphology

The FE-SEM images of PRA-MCM-48, pure TiO_2 , and $\text{TiO}_2/\text{PRA-MCM-48}$ are displayed in Fig. 11. Fig. 11(a) and (b) shows the surface morphology of PRA-MCM-48 synthesized at pH 11; mainly rectangular particle shapes with grain sizes of $0.4\text{--}0.6\text{ }\mu\text{m}$ [28]. As shown in Fig. 11(c), in a pure TiO_2 sample these particles were homogeneous and aggregated compactly. Enlarging the SEM image in Fig. 11(c), Fig. 11(d) demonstrates the stick-like morphology of pure TiO_2 , with a width of approximately 20 nm . Fig. 11(e)–(h) displays the SEM images of the 90% and 70% $\text{TiO}_2/\text{PRA-MCM-48}$ samples. The TiO_2 particles aggregated on the surface of PRA-MCM-48, as

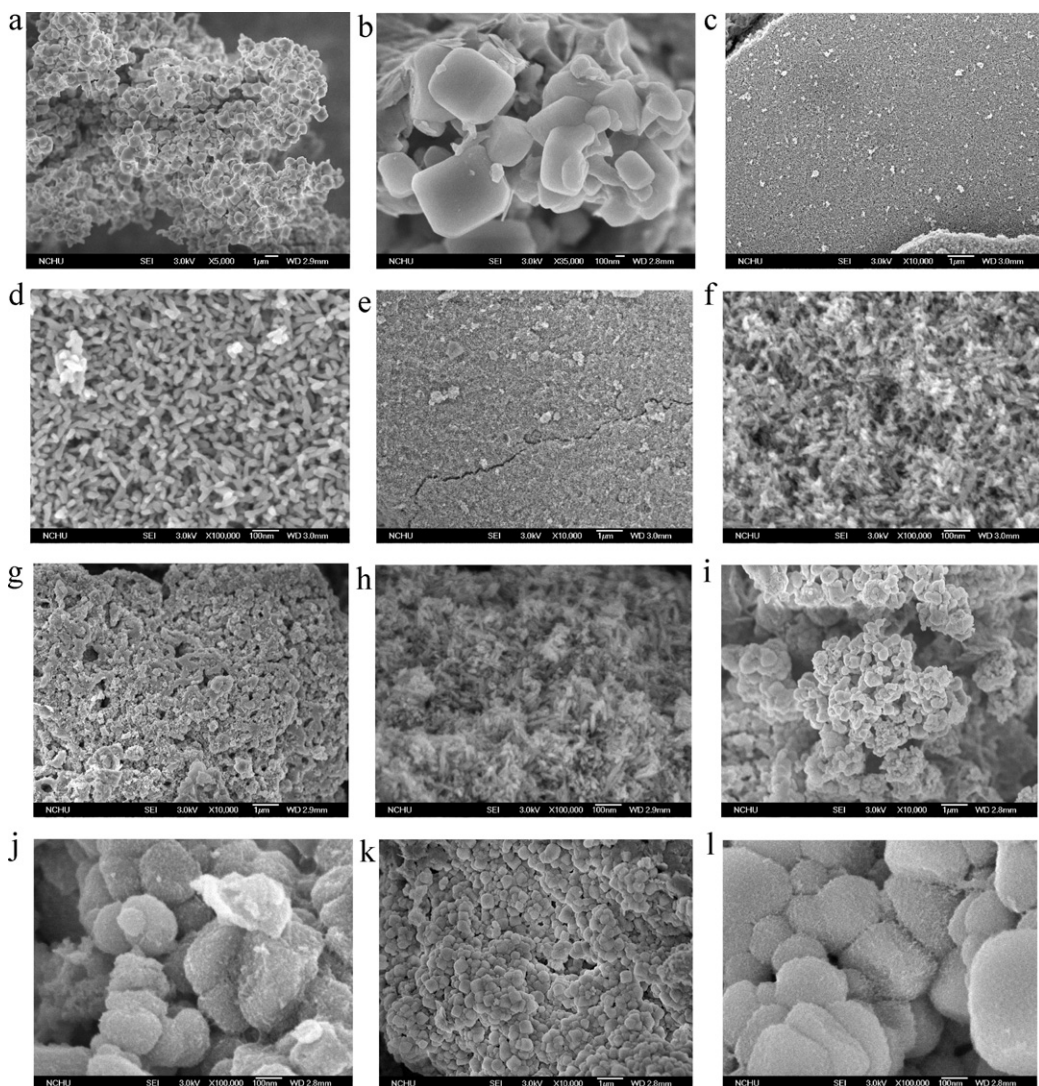


Fig. 11. FE-SEM images of PRA-MCM-48, pure TiO_2 , and $\text{TiO}_2/\text{PRA-MCM-48}$ samples: (a) and (b) PRA-MCM-48 silica synthesized at pH 11; (c) and (d) pure TiO_2 ; $\text{TiO}_2/\text{PRA-MCM-48}$ for various molar ratios of (e) and (f) 90%, (g) and (h) 70%, (i) and (j) 50%, and (k) and (l) 30%, respectively.

observed in Fig. 11(e) and (g). Fig. 11(f) and (h) shows the TiO_2 particles in acicular grain form with a mean width of 5 nm for 70% $\text{TiO}_2/\text{PRA-MCM-48}$ sample and 10 nm for 90% $\text{TiO}_2/\text{PRA-MCM-48}$ sample. The sizes of TiO_2 particles loaded on PRA-MCM-48 were smaller than those of pure TiO_2 . The low surface areas and pore volumes of 90% and 70% TiO_2 -loaded PRA-MCM-48 samples in N_2 absorption-desorption analysis indicated that TiO_2 mainly located externally to the MCM-48 surface. The aggregation of TiO_2 on the external silica surface had the effect of decreasing TiO_2 dispersion. Fig. 11(i) and (l) displays the SEM images of the 50% and 30% $\text{TiO}_2/\text{PRA-MCM-48}$ samples. The PRA-MCM-48 particle outlines were distinguishable (Fig. 11(i) and (k)). Fig. 11(j) and (l) shows the very fine TiO_2 particles disseminated on the surface of PRA-MCM-48. The high dispersion of TiO_2 on the catalyst support prevented their agglomeration and increased the photocatalytic activity. The SEM analysis findings also reveal that TiO_2 particle sizes decreased with decreasing TiO_2 loading. In normal circumstances, the smaller the TiO_2 particle size, the higher the photocatalytic activity [38]. Excessive loading of TiO_2 has resulted in the large-sized of TiO_2 aggregation and the decreased catalyst surface area. The optimal condition for TiO_2 loaded on MCM-48 was less than 50%.

4. Conclusions

The present study synthesized mesoporous photocatalysts with high purity using cheap, recycled silica sourced from electronic packaging resin ash. The presence of the MCM-48 support increased the photoefficiency of the TiO_2 catalyst by preventing the TiO_2 particles from aggregating. A $\text{TiO}_2/\text{PRA-MCM-48}$ molar ratio of 30% and heat-treatment temperature of 700 °C provided optimum photocatalytic performances. TiO_2 nanoparticles, of mainly anatase type, disseminate on the MCM-48 surface. Compared with pure TiO_2 powders, the sizes of the TiO_2 particles deposited on MCM-48 decreased, to below 10 nm, with decreased TiO_2 loading. MCM-48 can increase the concentration of MB around the TiO_2 particles and consequently increase the TiO_2 photocatalytic ability. The proposed method for preparation of photocatalyst composites is potentially useful in the recycling and utilization of e-waste.

Acknowledgment

The author expresses thanks to the National Science Council of Taiwan for its financial support under Project No. NSC 97-2221-E-131-006.

Appendix A. Supplementary data

Supplementary data associated with this article can be found, in the online version, at doi:10.1016/j.apcatb.2011.12.020.

References

- [1] M.L. Fetterolf, H.V. Patel, J.M. Jennings, *J. Chem. Eng. Data* 48 (2003) 831–835.
- [2] A. Lundström, T. Snelling, P. Morsing, P. Gabrielsson, E. Senar, L. Olsson, *Appl. Catal. B: Environ.* 106 (2011) 273–279.
- [3] I.C. Tran, Felix, M. Bar, L. Weinhardt, Y. Zhang, C. Heske, *J. Am. Chem. Soc.* 132 (2010) 5789–5792.
- [4] Q. Zheng, H. Kang, J. Yun, J. Lee, J.H. Park, S. Baik, *ACS Nano* 5 (2011) 5088–5093.
- [5] Y. Shibata, D. Suzuki, S. Omori, R. Tanaka, A. Murakami, Y. Kataoka, K. Baba, R. Kamijo, T. Miyazaki, *Biomaterials* 31 (2010) 8546–8555.
- [6] Y. Segura, L. Chmielarz, P. Kustrowski, P. Cool, R. Dziembaj, E.F. Vansant, *Appl. Catal. B: Environ.* 61 (2005) 69–78.
- [7] M.A. Zanjanchi, H. Golmoejdeh, M. Arvand, *J. Hazard. Mater.* 169 (2009) 233–239.
- [8] T.W. Kim, P.W. Chung, V.S.Y. Lin, *Chem. Mater.* 22 (2010) 5093–5104.
- [9] W. Zhao, Q. Li, L. Wang, J. Chu, J. Qu, S. Li, T. Qi, *Langmuir* 26 (2010) 6982–6988.
- [10] K. Czechura, A. Sayari, *Chem. Mater.* 18 (2006) 4147–4150.
- [11] V.S. Narkhede, A.D. Toni, V.V. Narkhede, M. Guraya, J.W. (Hans) Niemantsverdriet, M.W.E. van den Berg, W. Grünert, H. Gies, *Microporous Mesoporous Mater.* 118 (2009) 52–60.
- [12] H.J. Kim, B. Han, Y.J. Kim, S.J. Yoa, *J. Aerosol. Sci.* 41 (2010) 987–997.
- [13] D. Chen, X. Bi, M. Liu, B. Huang, G. Sheng, J. Fu, *Chemosphere* 82 (2011) 1246–1252.
- [14] C. Ai, Y. Xiao, W. Wen, L. Yuan, *Powder Technol.* 210 (2011) 323–327.
- [15] T.H. Liou, *J. Hazard. Mater.* 103 (2003) 107–123.
- [16] J. Cui, L. Zhang, *J. Hazard. Mater.* 158 (2008) 228–256.
- [17] T.H. Liou, *Chem. Eng. J.* 98 (2004) 39–51.
- [18] K. Hashimoto, K. Wasada, M. Osaki, E. Shono, K. Adachi, N. Toukai, H. Kominami, Y. Kera, *Appl. Catal. B: Environ.* 30 (2001) 429–436.
- [19] S. Wang, Y. Shi, X. Ma, J. Gong, *ACS Appl. Mater. Interfaces* 3 (2011) 2154–2160.
- [20] G. Wittmann, K. Demeester, A. Dombi, J. Dewulf, H.V. Langenhove, *Appl. Catal. B: Environ.* 61 (2005) 47–57.
- [21] Y.J. Acosta-Silva, R. Nava, V. Hernández-Morales, S.A. Macías-Sánchez, M.L. Gómez-Herrera, B. Pawelec, *Appl. Catal. B: Environ.* 110 (2011) 108–117.
- [22] E. Beyers, E. Biermans, S. Ribbens, K. De Witte, M. Mertens, V. Meynen, S. Bals, G. Van Tendeloo, E.F. Vansant, P. Cool, *Appl. Catal. B: Environ.* 88 (2009) 515–524.
- [23] D. Fattakhova-Rohlfing, J.M. Szeifert, Q. Yu, V. Kalousek, J. Rathouský, T. Bein, *Chem. Mater.* 21 (2009) 2410–2417.
- [24] X. Wang, Y. Liu, Z. Hu, Y. Chen, W. Liu, G. Zhao, *J. Hazard. Mater.* 169 (2009) 1061–1067.
- [25] J.W. Shi, S.H. Chen, S.M. Wang, Z.L. Ye, P. Wu, B. Xu, *J. Mol. Catal. A: Chem.* 330 (2010) 41–48.
- [26] D.I. Petkowicz, R. Brambilla, C. Radtke, C.D.S. da Silva, Z.N. da Rocha, S.B.C. Pergher, J.H.Z. dos Santos, *Appl. Catal. A: Gen.* 357 (2009) 125–134.
- [27] A.M. Doyle, E. Ahmed, B.K. Hodnett, *Catal. Today* 116 (2006) 50–55.
- [28] F.Y. Wei, Z.W. Liu, J. Lu, Z.T. Liu, *Microporous Mesoporous Mater.* 131 (2010) 224–229.
- [29] M. Bandyopadhyay, A. Birkner, M.W.E. van den Berg, K.V. Clementiev, W. Schmidt, W. Grünert, H. Gies, *Chem. Mater.* 17 (2005) 3820–3829.
- [30] D. Zhao, S. Budhi, A. Rodriguez, R.T. Koodali, *Int. J. Hydrogen Energy* 35 (2010) 5276–5283.
- [31] C.J. Brinker, G.W. Scherer, *Sol-Gel Science The Physics and Chemistry of Sol-Gel Processing*, Academic Press, Inc., San Diego, CA, 1990.
- [32] T.H. Liou, *Chem. Eng. J.* 171 (2011) 1458–1468.
- [33] C. Su, B.Y. Hong, C.M. Tseng, *Catal. Today* 96 (2004) 119–126.
- [34] G. Zhang, J. Yi, J. Shim, J. Lee, W. Choi, *Appl. Catal. B: Environ.* 102 (2011) 132–139.
- [35] S. Han, J. Xu, W. Hou, X. Yu, Y. Wang, *J. Phys. Chem. B* 108 (2004) 15043–15048.
- [36] S. Muto, H. Imai, *Microporous Mesoporous Mater.* 95 (2006) 200–205.
- [37] Y. Li, X. Li, J. Li, J. Yin, *Water Res.* 40 (2006) 1119–1126.
- [38] X. Wang, Z. Hu, Y. Chen, G. Zhao, Y. Liu, Z. Wen, *Appl. Surf. Sci.* 255 (2009) 3953–3958.
- [39] S. Artkla, W. Kim, W. Choi, J. Wittayakun, *Appl. Catal. B: Environ.* 91 (2009) 157–164.
- [40] X. Liu, Y. Du, Z. Guo, S. Gunasekaran, C.B. Ching, Y. Chen, S.S.J. Leong, Y. Yang, *Microporous Mesoporous Mater.* 122 (2009) 114–120.
- [41] K.S.W. Sing, D.H. Everett, R.A.W. Haul, L. Moscou, R.A. Pierotti, J. Rouquerol, T. Siemieniewska, *Pure Appl. Chem.* 57 (1985) 603–619.
- [42] M. Hussain, R. Ceccarelli, D.L. Marchisio, D. Fino, N. Russo, F. Geobaldo, *Chem. Eng. J.* 157 (2010) 45–51.
- [43] J. Yang, J. Zhang, L. Zhu, S. Chen, Y. Zhang, Y. Tang, Y. Zhua, Y. Li, *J. Hazard. Mater.* 137 (2006) 952–958.
- [44] W. Wang, M. Song, *Microporous Mesoporous Mater.* 96 (2006) 255–261.
- [45] C. Anderson, A.J. Bard, *J. Phys. Chem.* 99 (1995) 9882–9885.
- [46] S. Anandan, *Dyes Pigments* 76 (2008) 535–541.
- [47] T.H. Liou, C.C. Yang, *Mater. Sci. Eng. B: Adv.* 176 (2011) 521–529.
- [48] X. Wang, W. Lian, X. Fu, J.M. Basset, F. Lefebvre, *J. Catal.* 238 (2006) 13–20.
- [49] J. Jitputti, S. Pavasupree, Y. Suzuki, S. Yoshikawa, *J. Solid State Chem.* 180 (2007) 1743–1749.